Integrated simulation of the injection molding process with stereolithography molds

Abstract Functional parts are needed for design verification testing, field trials, customer evaluation, and production plan ning. By eliminating multiple steps, the creation of the injec tion mold directly by a rapid prototyping (RP) process holds the best promise of reducing the time and cost needed to mold low-volume quantities of parts. The potential of this integra tion of injection molding with RP has been demonstrated many times. What is missing is the fundamental understanding of how the modifications to the mold material and RP manufacturing process impact both the mold design and the injection mold ing process. In addition, numerical simulation techniques have now become helpful tools of mold designers and process engi neers for traditional injection molding. But all current simulation packages for conventional injection molding are no longer ap plicable to this new type of injection molds, mainly because the property of the mold material changes greatly. In this paper, an integrated approach to accomplish a numerical simulation of in jection molding into rapid-prototyped molds is established and a corresponding simulation system is developed. Comparisons with experimental results are employed for verification, which show that the present scheme is well suited to handle RP fabri cated stereolithography (SL) molds.

Keywords Injection molding Numerical simulation Rapid prototyping

1 Introduction

In injection molding, the polymer melt at high temperature is injected into the mold under high pressure [1]. Thus, the mold material needs to have thermal and mechanical properties capa ble of withstanding the temperatures and pressures of the mold ing cycle. The focus of many studies has been to create the

injection mold directly by a rapid prototyping (RP) process. By eliminating multiple steps, this method of tooling holds the best promise of reducing the time and cost needed to create low-volume quantities of parts in a production material. The potential of integrating injection molding with RP technologies has been demonstrated many times. The properties of RP molds are very different from those of traditional metal molds. The key differ ences are the properties of thermal conductivity and elastic mod ulus (rigidity). For example, the polymers used in

RP-fabricated stereolithography (SL) molds have a thermal conductivity that is less than one thousandth that of an aluminum tool. In using RP technologies to create molds, the entire mold design and injection-molding process parameters need to be modified and optimized from traditional methodologies due to the completely different tool material. However, there is still not a fundamental understanding of how the modifications to the mold tooling method and material impact both the mold design and the injection molding process parameters. One cannot obtain reasonable results by simply changing a few material properties in current models. Also, using traditional approaches when making actual parts may be generating sub-optimal results. So there is a dire need to study the interaction between the rapid tooling (RT) process and material and injection molding, so as to establish the mold design criteria and techniques for an RT-oriented injection molding process.

In addition, computer simulation is an effective approach for predicting the quality of molded parts. Commercially available simulation packages of the traditional injection molding process have now become routine tools of the mold designer and process engineer [2]. Unfortunately, current simulation programs for conventional injection molding are no longer applicable to RP molds, because of the dramatically dissimilar tool material. For instance, in using the existing simulation software with aluminum and SL molds and comparing with experimental results, though the simulation values of part distortion are reasonable for the aluminum mold, results are unacceptable, with the error exceeding 50%. The distortion during injection molding is due to shrinkage and warpage of the plastic part, as well as the mold. For ordinarily molds, the main factor is the shrinkage and warpage of the plastic part, which is modeled accurately in current simulations. But for RP molds, the distortion of the mold has potentially more influence, which have been neglected in current models. For instance, [3] used a simple three-step simulation process to consider the mold distortion, which had too much deviation.

In this paper, based on the above analysis, a new simulation system for RP molds is developed. The proposed system focuses on predicting part distortion, which is dominating defect in RP-molded parts. The developed simulation can be applied as an evaluation tool for RP mold design and process optimization. Our simulation system is verified by an experimental example.

Although many materials are available for use in RP technologies, we concentrate on using stereolithography (SL), the original RP technology, to create

polymer molds. The SL pro cess uses photopolymer and laser energy to build a part layer by layer. Using SL takes advantage of both the commercial domi nance of SL in the RP industry and the subsequent expertise base that has been developed for creating accurate, high-quality parts. Until recently, SL was primarily used to create physical models for visual inspection and form-fit studies with very limited func tional applications. However, the newer generation stereolitho graphic photopolymers have improved dimensional, mechanical and thermal properties making it possible to use them for actual functional molds.

2 Integrated simulation of the molding process

2.1 Methodology

In order to simulate the use of an SL mold in the injection molding process, an iterative method is proposed. Different soft ware modules have been developed and used to accomplish this task. The main assumption is that temperature and load bound ary conditions cause significant distortions in the SL mold. The simulation steps are as follows:

1 The part geometry is modeled as a solid model, which is translated to a file readable by the flow analysis package.

2 Simulate the mold-filling process of the melt into a pho topolymer mold, which will output the resulting temperature and pressure profiles.

3 Structural analysis is then performed on the photopolymer mold model using the thermal and load boundary conditions obtained from the previous step, which calculates the distor tion that the mold undergo during the injection process.

4 If the distortion of the mold converges, move to the next step. Otherwise, the distorted mold cavity is then modeled (changes in the dimensions of the cavity after distortion), and returns to the second step to simulate the melt injection into the distorted mold.

5 The shrinkage and warpage simulation of the injection molded part is then applied, which calculates the final distor tions of the molded part.

In above simulation flow, there are three basic simulation mod ules.

2. 2 Filling simulation of the melt

2.2.1 Mathematical modeling

In order to simulate the use of an SL mold in the injection molding process, an iterative method is proposed. Different software modules have been developed and used to accomplish this task. The main assumption is that temperature and load boundary conditions cause significant distortions in the SL mold. The simulation steps are as follows:

1. The part geometry is modeled as a solid model, which is translated to a file readable by the flow analysis package.

2. Simulate the mold-filling process of the melt into a photopolymer mold, which will output the resulting temperature and pressure profiles.

3. Structural analysis is then performed on the photopolymer mold model using the thermal and load boundary conditions obtained from the previous step, which calculates the distortion that the mold undergo during the injection process.

4. If the distortion of the mold converges, move to the next step. Otherwise, the distorted mold cavity is then modeled (changes in the dimensions of the cavity after distortion), and returns to the second step to simulate the melt injection into the distorted mold.

5. The shrinkage and warpage simulation of the injection molded part is then applied, which calculates the final distortions of the molded part.

In above simulation flow, there are three basic simulation modules.

2.2 Filling simulation of the melt

2.2.1 Mathematical modeling

Computer simulation techniques have had success in predicting filling behavior in extremely complicated geometries. However, most of the current numerical implementation is based on a hybrid finite-element/finite-difference solution with the middleplane model. The application process of simulation packages based on this model is illustrated in Fig. 2-1. However, unlike the surface/solid model in mold-design CAD systems, the so-called middle-plane (as shown in Fig. 2-1b) is an imaginary arbitrary planar geometry at the middle of the cavity in the gap-wise direction, which should bring about great inconvenience in applications. For example, surface models are commonly used in current RP systems (generally STL file format), so secondary modeling is unavoidable when using simulation packages because the models in the RP and simulation systems are different. Considering these defects, the

surface model of the cavity is introduced as datum planes in the simulation, instead of the middle-plane.

According to the previous investigations [4–6], fillinggoverning equations for the flow and temperature field can be written as:

$$\frac{\partial(b\overline{u})}{\partial x}+\frac{\partial(b\overline{v})}{\partial y}=0 \tag{1}$$

$$\frac{\partial P}{\partial x}-\frac{\partial}{\partial z}\left(\eta\frac{\partial u}{\partial z}\right)=0 \tag{2}$$

$$\frac{\partial P}{\partial y}-\frac{\partial}{\partial z}\left(\eta\frac{\partial v}{\partial z}\right)=0 \tag{3}$$

$$\rho C_P\left(\frac{\partial T}{\partial t}+u\frac{\partial T}{\partial x}+v\frac{\partial T}{\partial y}\right)=K\frac{\partial^2 T}{\partial z^2}+\eta\left[\left(\frac{\partial u}{\partial x}\right)^2+\left(\frac{\partial v}{\partial y}\right)^2\right] \tag{4}$$

where *x, y* are the planar coordinates in the middle-plane, and *z* is the gap-wise coordinate; *u, v,w* are the velocity components in the *x, y, z* directions; *u, v* are the average whole-gap thicknesses; and *η, ρ,CP (T), K(T)* represent viscosity, density, specific heat and thermal conductivity of polymer melt, respectively.

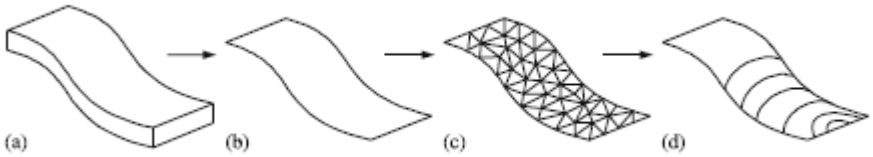

Fig.2-1 a–d. Schematic procedure of the simulation with middle-plane model. **a** The 3-D surface model **b** The middle-plane model **c** The meshed middle-plane model **d** The display of the simulation result

In addition, boundary conditions in the gap-wise direction can be defined as:

$$u=w=v=0,\ T=T_W \qquad \text{at } z=b \tag{5}$$

$$\frac{\partial u}{\partial z}=0=\frac{\partial v}{\partial z},\ \frac{\partial T}{\partial z}=0,\ w=0 \ \text{ at } z=0 \tag{6}$$

where *TW* is the constant wall temperature (shown in Fig. 2a).

Combining Eqs. 1–4 with Eqs. 5–6, it follows that the distributions of the *u, v, T, P* at *z* coordinates should be symmetrical, with the mirror axis being *z* = 0, and consequently the *u, v* averaged in half-gap thickness is equal to that averaged in wholegap thickness. Based on this characteristic, we can divide the whole cavity into two equal parts in the gap-wise direction, as described by *Part I* and *Part II* in Fig. 2b. At the same time, triangular finite elements are generated in the surface(s) of the cavity (at *z* = 0 in Fig. 2b), instead of the middle-plane (at *z* = 0 in Fig. 2a).

Accordingly, finite-difference increments in the gapwise direction are employed only in the inside of the surface(s) (wall to middle/center-line), which, in Fig. 2b, means from $z = 0$ to $z = b$. This is single-sided instead of two-sided with respect to the middle-plane (i.e. from the middle-line to two walls). In addition, the coordinate system is changed from Fig. 2a to Fig. 2b to alter the finite-element/finite-difference scheme, as shown in Fig. 2b. With the above adjustment, governing equations are still Eqs. 1–4. However, the original boundary conditions in the gapwise direction are rewritten as:

$$u = w = v = 0,\ T = T_W \qquad \text{at } z = 0 \tag{7}$$

$$\frac{\partial u}{\partial z} = 0 = \frac{\partial v}{\partial z},\ \frac{\partial T}{\partial z} = 0,\ w = 0 \ \text{at } z = b \tag{8}$$

Meanwhile, additional boundary conditions must be employed at $z = b$ in order to keep the flows at the juncture of the two parts at the same section coordinate [7]:

$$u_I = u_{II};\ v_I = v_{II};\ T_I = T_{II};\ P_I = P_{II} \qquad \text{at } z = b \tag{9}$$

$$Cm - I = Cm - II \tag{10}$$

where subscripts I, II represent the parameters of *Part I* and *Part II*, respectively, and Cm-I and Cm-II indicate the moving free melt-fronts of the surfaces of the divided two parts in the filling stage.

It should be noted that, unlike conditions Eqs. 7 and 8, ensuring conditions Eqs. 9 and 10 are upheld in numerical implementations becomes more difficult due to the following reasons:

1. The surfaces at the same section have been meshed respectively, which leads to a distinctive pattern of finite elements at the same section. Thus, an interpolation operation should be employed for *u, v, T, P* during the comparison between the two parts at the juncture.

2. Because the two parts have respective flow fields with respect to the nodes at point A and point C (as shown in Fig. 2b) at the same section, it is possible to have either both filled or one filled (and one empty). These two cases should be handled separately, averaging the operation for the former, whereas assigning operation for the latter.

3. It follows that a small difference between the melt-fronts is permissible. That allowance can be implemented by time allowance control or preferable location allowance control of the melt-front nodes.

4. The boundaries of the flow field expand by each melt-front advancement, so it

is necessary to check the condition Eq. 10 after each change in the melt-front.

5. In view of above-mentioned analysis, the physical parameters at the nodes of the same section should be compared and adjusted, so the information describing finite elements of the same section should be prepared before simulation, that is, the matching operation among the elements should be preformed.

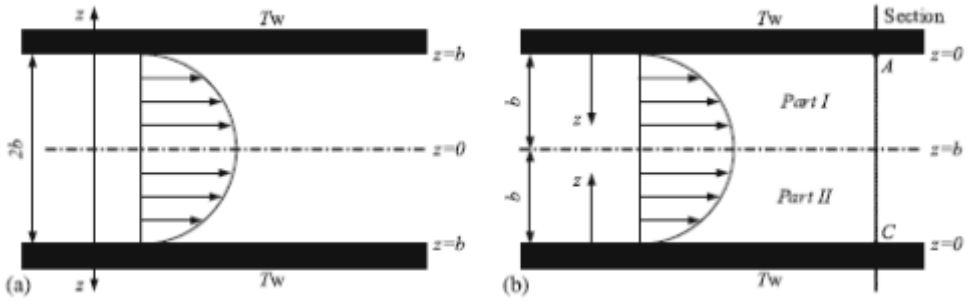

Fig. 2a,b. Illustrative of boundary conditions in the gap-wise direction **a** of the middle-plane model **b** of the surface model

2.2.2 Numerical implementation

Pressure field. In modeling viscosity η, which is a function of shear rate, temperature and pressure of melt, the shear-thinning behavior can be well represented by a cross-type model such as:

$$\eta(\dot{\gamma}, T, P) = \frac{\eta_0(T, P)}{1 + \left(\eta_0 \dot{\gamma} / \tau^*\right)^{1-n}} \tag{11}$$

where n corresponds to the power-law index, and τ^* characterizes the shear stress level of the transition region between the Newtonian and power-law asymptotic limits. In terms of an

Arrhenius-type temperature sensitivity and exponential pressure dependence, $\eta 0(T, P)$ can be represented with reasonable accuracy as follows:

$$\eta_0(T, P) = Be^{\beta P} e^{T_b/T} \tag{12}$$

Equations 11 and 12 constitute a five-constant (n, τ^* , B, Tb, β) representation for viscosity. The shear rate for viscosity calculation is obtained by:

$$\dot{\gamma} = \sqrt{\left(\frac{\partial u}{\partial z}\right)^2 + \left(\frac{\partial v}{\partial z}\right)^2} \tag{13}$$

Based on the above, we can infer the following filling pressure equation from the governing Eqs. 1–4:

$$\nabla \bullet (S \nabla P) = 0 \tag{14}$$

where S is calculated by $S = \int_0^{b} /(b-z)2\ \eta\ \mathrm{d}z$. Applying the Galerkin method, the pressure finite-element equation is deduced as:

$$\sum_{l} S^{(l)} \sum_{j=1}^{3} D_{ij}^{(l)} P_{N'} = 0 \tag{15}$$

where $l\_$ traverses all elements, including node N, and where I and j represent the local node number in element $l\_$ corresponding to the node number N and $N\_$ in the whole, respectively. The $D(l\_)\ ij$ is calculated as follows:

$$D_{ij}^{(l)} = \int_{A^{(l)}} [\nabla L_i^{(l)}(x, y) \bullet \nabla L_j^{(l)}(x, y)] \mathrm{d}A \tag{16}$$

where $A(l\_)$ represents triangular finite elements, and $L(l\_)\ i$ is the pressure trial function in finite elements.

Temperature field. To determine the temperature profile across the gap, each triangular finite element at the surface is further divided into NZ layers for the finite-difference grid.

The left item of the energy equation (Eq. 4) can be expressed as:

$$\rho C_P \frac{\partial T}{\partial t}\Big|_{N,j,t+1} = \rho C_P \frac{T_{N,j,t+1} - T_{N,j,t}}{\Delta t} \qquad j = 1, 2, 3, \cdots, NZ \tag{17}$$

where TN, j, t represents the temperature of the j layer of node N at time t. The heat conduction item is calculated by:

$$K \frac{\partial^2 T}{\partial z^2}\Big|_{N,j,t+1} = \frac{1}{\sum_l V_{i,j}^{(l)}} \times \sum_l \left\{ \frac{V_{i,l}^{(l)} K}{3\Delta z_j^2} \left[\sum_{m=1}^{3} (T_{N',j+1,t+1} - 2T_{N',j,t+1} + T_{N',j-1,t+1}) \right] \right\} \qquad j = 1, 2, 3, \cdots, NZ \tag{18}$$

where l traverses all elements, including node N, and i and j represent the local node number in element l corresponding to the node number N and $N\_$ in the whole, respectively.

The heat convection item is calculated by:

$$\rho C_P \left(u\frac{\partial T}{\partial x} + v\frac{\partial T}{\partial y}\right)\Big|_{N,j,t+1} = \frac{\rho C_P}{\sum_l V_{i,j}^{(l)}} \sum_l \left\{ V_{i,j}^{(l)} \frac{\int_{-b}^{z_j} \left(\frac{\tilde{z}}{\eta}\right)^{(l)} d\tilde{z}}{2A^{(l)}} \times \sum_{m=1}^{3} \left[\left(-\frac{\partial P}{\partial x}\right)^{(l)} b_{2m}^{(l)} + \left(-\frac{\partial P}{\partial y}\right)^{(l)} b_{3m}^{(l)} \right] \cdot T_{N^r,j,t+1} \right\}$$
$$j = 1, 2, 3, \cdots, NZ \tag{19}$$

For viscous heat, it follows that:

$$\eta\dot{\gamma}^2\Big|_{N,j,t+1} = \frac{1}{\sum_l V_{i,j}^{(l)}} \sum_l V_{i,j}^{(l)} \cdot \left[z_j \sqrt{\left(\frac{\partial P}{\partial x}\right)^2 + \left(\frac{\partial P}{\partial y}\right)^2}^{(l)} \right]^2 \cdot \frac{1}{\eta^{(l)}}$$
$$j = 1, 2, 3, \cdots, NZ \tag{20}$$

Substituting Eqs. 17–20 into the energy equation (Eq. 4), the temperature equation becomes:

$$[K]\{T\} = \{F\} \tag{21}$$

2.3 Structural analysis of the mold

The purpose of structural analysis is to predict the deformation occurring in the photopolymer mold due to the thermal and mechanical loads of the filling process. This model is based on a three-dimensional thermoelastic boundary element method (BEM). The BEM is ideally suited for this application because only the deformation of the mold surfaces is of interest. Moreover, the BEM has an advantage over other techniques in that computing effort is not wasted on calculating deformation within the mold.

The stresses resulting from the process loads are well within the elastic range of the mold material. Therefore, the mold deformation model is based on a thermoelastic formulation. The thermal and mechanical properties of the mold are assumed to be isotropic and temperature independent.

Although the process is cyclic, time-averaged values of temperature and heat flux are used for calculating the mold deformation. Typically, transient temperature variations within a mold have been restricted to regions local to the cavity surface and the nozzle tip [8]. The transients decay sharply with distance from the cavity surface and generally little variation is observed beyond distances as small as 2.5 mm. This suggests that the contribution from the transients to the deformation at the mold block interface is small, and therefore it is reasonable to neglect the transient effects. The

steady state temperature field satisfies Laplace's equation $2T = 0$ and the time-averaged boundary conditions. The boundary conditions on the mold surfaces are described in detail by Tang et al. [9]. As for the mechanical boundary conditions, the cavity surface is subjected to the melt pressure, the surfaces of the mold connected to the worktable are fixed in space, and other external surfaces are assumed to be stress free.

The derivation of the thermoelastic boundary integral formulation is well known [10]. It is given by:

$$c_{lk}(x)u_k(x) + \int_\Gamma \tilde{p}_{lk}(x, y)u_k(y)y\,d\Gamma(y) = \int_\Gamma \tilde{u}_{lk}(x, y)\,p_k(y)\,d\Gamma(y) + \frac{\alpha(1+\nu)}{8\pi(1-\nu)}\int_\Gamma \left[\frac{\partial r_{,l}}{\partial n}T(y) - r_{,l}\frac{\partial T}{\partial n}(y)\right]y\,d\Gamma(y) \qquad (22)$$

where uk, pk and T are the displacement, traction and temperature, α, ν represent the thermal expansion coefficient and Poisson's ratio of the material, and $r = |y-x|$. $clk(x)$ is the surface coefficient which depends on the local geometry at x, the orientation of the coordinate frame and Poisson's ratio for the domain [11]. The fundamental displacement $\tilde{}ulk$ at a point y in the xk direction, in a three-dimensional infinite isotropic elastic domain, results from a unit load concentrated at a point x acting in the xl direction and is of the form:

$$\tilde{u}_{lk} = \frac{1}{16\pi\mu(1-\nu)r}[(3-4\nu)\delta_{lk} + r_{,l}r_{,k}] \qquad (23)$$

where δlk is the Kronecker delta function and μ is the shear modulus of the mold material.

The fundamental traction $\tilde{}plk$, measured at the point y on a surface with unit normal $\mathbf{n}$, is:

$$\tilde{p}_{lk} = \frac{2\nu-1}{8\pi(1-\nu)r^2}\left[\frac{\partial r}{\partial n}\left(\delta_{lk} + \frac{3r_{,l}r_{,k}}{1-2\nu}\right) + n_l r_{,k} - n_k r_{,l}\right] \qquad (24)$$

Discretizing the surface of the mold into a total of N elements transforms Eq. 22 to:

$$c_{lk}(x)u_k(x)+\sum_{n=1}^{N}\int_{\Gamma_n}\tilde{p}_{lk}(x,y)u_k(y)\mathrm{d}\Gamma(y)$$
$$=\sum_{n=1}^{N}\int_{\Gamma_n}\tilde{u}_{lk}(x,y)p_k(y)\mathrm{d}\Gamma(y)$$
$$+\frac{\alpha(1+\nu)}{8\pi(1-\nu)}\sum_{n=1}^{N}\int_{\Gamma_n}\left[\frac{\partial r_{,l}}{\partial n}T(y)-r_{,l}\frac{\partial T}{\partial n}(y)\right]\mathrm{d}\Gamma(y) \quad (25)$$

where Γn refers to the nth surface element on the domain.

Substituting the appropriate linear shape functions into Eq. 25, the linear boundary element formulation for the mold deformation model is obtained. The equation is applied at each node on the discretized mold surface, thus giving a system of $3N$ linear equations, where N is the total number of nodes. Each node has eight associated quantities: three components of displacement, three components of traction, a temperature and a heat flux. The steady state thermal model supplies temperature and flux values as known quantities for each node, and of the remaining six quantities, three must be specified. Moreover, the displacement values specified at a certain number of nodes must eliminate the possibility of a rigid-body motion or rigid-body rotation to ensure a non-singular system of equations. The resulting system of equations is assembled into a integrated matrix, which is solved with an iterative solver.

2.4 Shrinkage and warpage simulation of the molded part

Internal stresses in injection-molded components are the principal cause of shrinkage and warpage. These residual stresses are mainly frozen-in thermal stresses due to inhomogeneous cooling, when surface layers stiffen sooner than the core region, as in free quenching. Based on the assumption of the linear thermo-elastic and linear thermo-viscoelastic compressible behavior of the polymeric materials, shrinkage and warpage are obtained implicitly using displacement formulations, and the governing equations can be solved numerically using a finite element method.

With the basic assumptions of injection molding [12], the components of stress and strain are given by:

$$\begin{cases}\sigma_{xy}=\sigma_{yx}=\sigma_{xz}=\sigma_{zx}=\sigma_z=0\\ \sigma_x(z,t)=\sigma_y(z,t)=\sigma_x(X,t)=\sigma_y(X,t)=\sigma(z,t)\\ \varepsilon_z(X,t)=\varepsilon_z(z,t)\\ \varepsilon_y(X,t)=\varepsilon_x(X,t)=\varepsilon(t)\end{cases} \quad (26)$$

The deviatoric components of stress and strain, respectively, are given by

$$\begin{cases} s_x = s_y = -\frac{s_z}{2} = \frac{\sigma(z,t)}{3} \\ e_x = e_y = -\frac{e_z}{2} = \frac{\varepsilon(t)-\varepsilon_z(z,t)}{3} \end{cases} \tag{27}$$

Using a similar approach developed by Lee and Rogers [13] for predicting the residual stresses in the tempering of glass, an integral form of the viscoelastic constitutive relationships is used, and the in-plane stresses can be related to the strains by the following equation:

$$\sigma(z,\xi) = \int_{-\infty}^{\xi} G_1(\xi-\xi')\frac{\partial}{\partial\xi'}\left[\varepsilon(\xi') - \varepsilon_z(z,\xi')\right] \mathrm{d}\xi' \tag{28}$$

Where $G1$ is the relaxation shear modulus of the material. The dilatational stresses can be related to the strain as follows:

$$\sigma_{kk} = 3G_2[\varepsilon_{kk} - \alpha\Theta] \tag{29}$$

Where K is the relaxation bulk modulus of the material, and the definition of α and Θ is:

$$\Theta(x,t) = \frac{1}{\alpha_0}\int_{T_0}^{T} \alpha(t)\,\mathrm{d}T,\ \alpha_0 = \alpha(T_0) \tag{30}$$

If $\alpha(t) = \alpha 0$, applying Eq. 27 to Eq. 29 results in:

$$2\sigma(z,\xi) = 3G_2\{2\varepsilon(\xi) + \varepsilon_z(z,\xi) - 3\alpha_0[T(z,\xi) - T(z,0)]\} \tag{31}$$

Similarly, applying Eq. 31 to Eq. 28 and eliminating strain $\varepsilon xx(z, t)$ results in:

$$\begin{aligned} &\frac{4}{3G_2}\int_{-\infty}^{\xi} G_1(\xi-\xi')\frac{\partial}{\partial\xi'}[\sigma(z,\xi')]\,\mathrm{d}\xi' + \sigma(z,\xi) \\ &= 3\int_{-\infty}^{\xi} 2G_1(\xi-\xi')\frac{\partial}{\partial\xi'}[\varepsilon(\xi') - \alpha_0(T(z,\xi') - T(z,0))]\,\mathrm{d}\xi' \end{aligned} \tag{32}$$

Employing a Laplace transform to Eq. 32, the auxiliary modulus $R(\xi)$ is given by:

$$\frac{4}{3G_2}\int_{-\infty}^{\xi} G_1(\xi-\xi')\frac{\partial R(\xi')}{\partial\xi'}\mathrm{d}\xi' + R(\xi) = 2G_1(\xi) \tag{33}$$

Using the above constitutive equation (Eq. 33) and simplified forms of the stresses and strains in the mold, the formulation of the residual stress of the injection molded part during the cooling stage is obtain by:

$$\sigma(z,\xi)=3\int_{-\infty}^{\xi}R(\xi-\xi')\frac{\partial}{\partial\xi'}[\varepsilon(z,\xi')-\alpha_0 T(z,\xi')]\,\mathrm{d}\xi' \qquad (34)$$

Equation 34 can be solved through the application of trapezoidal quadrature. Due to the rapid initial change in the material time, a quasi-numerical procedure is employed for evaluating the integral item. The auxiliary modulus is evaluated numerically by the trapezoidal rule.

For warpage analysis, nodal displacements and curvatures for shell elements are expressed as:

$$\{r_e\}=[k]\{d\}=\int_v [B_e]^T[D][B_e]\,\mathrm{d}v_e\{d\} \qquad (35)$$

where $[k]$ is the element stiffness matrix, $[Be]$ is the derivative operator matrix, $\{d\}$ is the displacements, and $\{re\}$ is the element load vector which can be evaluated by:

$$\{r_e\}=\int_v [B_e]^T[D][\varepsilon_0]\,\mathrm{d}v_e-\int_v [B_e]^T[\sigma_t]\,\mathrm{d}v_e \qquad (36)$$

The use of a full three-dimensional FEM analysis can achieve accurate warpage results, however, it is cumbersome when the shape of the part is very complicated. In this paper, a twodimensional FEM method, based on shell theory, was used because most injection-molded parts have a sheet-like geometry in which the thickness is much smaller than the other dimensions of the part. Therefore, the part can be regarded as an assembly of flat elements to predict warpage. Each three-node shell element is a combination of a constant strain triangular element (CST) and a discrete Kirchhoff triangular element (DKT), as shown in Fig. 3. Thus, the warpage can be separated into plane-stretching deformation of the CST and plate-bending deformation of the DKT, and correspondingly, the element stiffness matrix to describe warpage can also be divided into the stretching-stiffness matrix and bending-stiffness matrix.

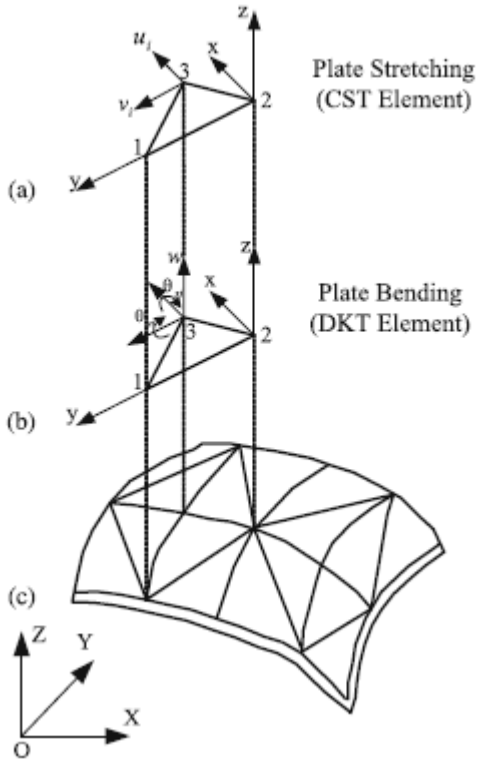

Fig. 3a–c. Deformation decomposition of shell element in the local coordinate system. **a** In-plane stretching element **b** Plate-bending element **c** Shell element

3 Experimental validation

To assess the usefulness of the proposed model and developed program, verification is important. The distortions obtained from the simulation model are compared to the ones from SL injection molding experiments whose data is presented in the literature [8]. A common injection molded part with the dimensions of 36×36×6 mm is considered in the experiment, as shown in Fig. 4. The thickness dimensions of the thin walls and rib are both 1.5 mm; and polypropylene was used as the injection material. The injection machine was a production level ARGURY Hydronica 320-210-750 with the following process parameters: a melt temperature of 250 ◦C; an ambient temperature of 30 ◦C; an injection pressure of 13.79 MPa; an injection time of 3 s; and a cooling time of 48 s. The SL material used, Dupont SOMOSTM 6110 resin, has the ability to resist temperatures of up to 300 ◦C temperatures. As mentioned above, thermal conductivity of the mold is a major factor that differentiates between an SL and a traditional mold. Poor heat transfer in the mold would produce a non-uniform temperature distribution, thus causing warpage that distorts the

completed parts. For an SL mold, a longer cycle time would be expected. The method of using a thin shell SL mold backed with a higher thermal conductivity metal (aluminum) was selected to increase thermal conductivity of the SL mold.

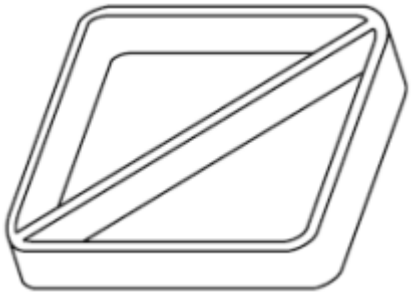

Fig. 4. Experimental cavity model

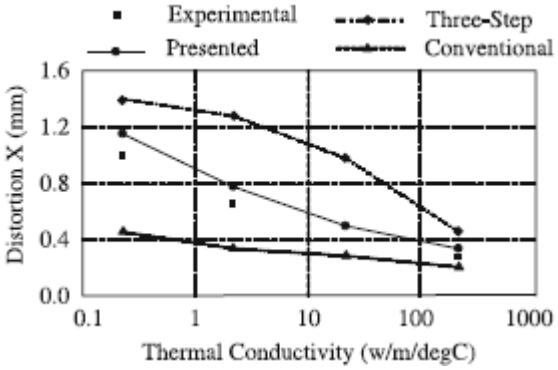

Fig. 5. A comparison of the distortion variation in the X direction for different thermal conductivity; where "Experimental", "present", "three-step", and "conventional" mean the results of the experimental, the presented simulation, the three-step simulation process and the conventional injection molding simulation, respectively.

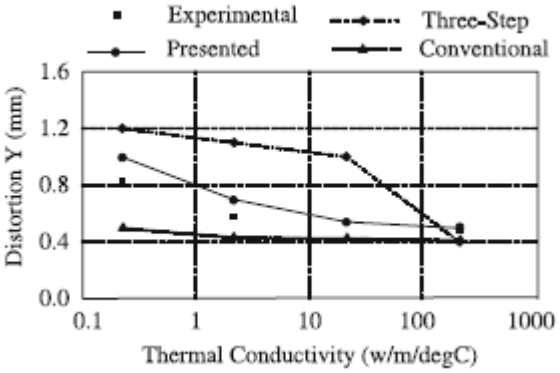

Fig. 6. Comparison of the distortion variation in the Y direction for different thermal conductivities

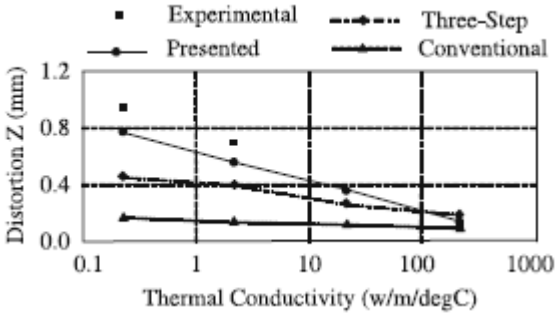

Fig. 7. Comparison of the distortion variation in the Z direction for different thermal conductivities

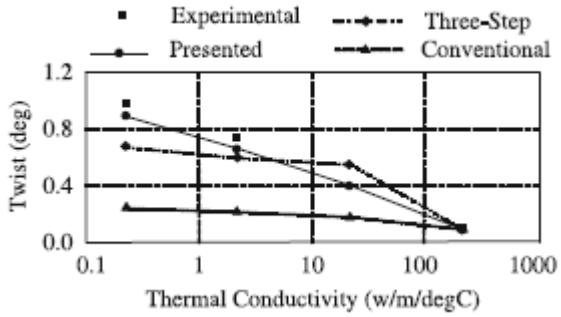

Fig. 8. Comparison of the twist variation for different thermal conductivities

For this part, distortion includes the displacements in three directions and the twist (the difference in angle between two initially parallel edges). The validation results are shown in Fig. 5 to Fig. 8. These figures also include the distortion values predicted by conventional injection molding simulation and the three-step model reported in [3].

4 Conclusions

In this paper, an integrated model to accomplish the numerical simulation of injection molding into rapid-prototyped molds is established and a corresponding simulation system is developed. For verification, an experiment is also carried out with an RPfabricated SL mold.

It is seen that a conventional simulation using current injection molding software breaks down for a photopolymer mold. It is assumed that this is due to the distortion in the mold caused by the temperature and load conditions of injection. The three-step approach also has much deviation. The developed model gives results closer to experimental.

Improvement in thermal conductivity of the photopolymer significantly increases

part quality. Since the effect of temperature seems to be more dominant than that of pressure (load), an improvement in the thermal conductivity of the photopolymer can improve the part quality significantly.

Rapid Prototyping (RP) is a technology makes it possible to manufacture prototypes quickly and inexpensively, regardless of their complexity. Rapid Tooling (RT) is the next step in RP's steady progress and much work is being done to obtain more accurate tools to define the parameters of the process. Existing simulation tools can not provide the researcher with a useful means of studying relative changes. An integrated model, such as the one presented in this paper, is necessary to obtain accurate predictions of the actual quality of final parts. In the future, we expect to see this work expanded to develop simulations program for injection into RP molds manufactured by other RT processes.

References

1. Wang KK (1980) System approach to injection molding process. Polym-Plast Technol Eng 14(1):75–93.
2. Shelesh-Nezhad K, Siores E (1997) Intelligent system for plastic injection molding process design. J Mater Process Technol 63(1–3):458–462.
3. Aluru R, Keefe M, Advani S (2001) Simulation of injection molding into rapid-prototyped molds. Rapid Prototyping J 7(1):42–51.
4. Shen SF (1984) Simulation of polymeric flows in the injection molding process. Int J Numer Methods Fluids 4(2):171–184.
5. Agassant JF, Alles H, Philipon S, Vincent M (1988) Experimental and theoretical study of the injection molding of thermoplastic materials. Polym Eng Sci 28(7):460–468.
6. Chiang HH, Hieber CA, Wang KK (1991) A unified simulation of the filling and post-filling stages in injection molding. Part I: formulation. Polym Eng Sci 31(2):116–124.
7. Zhou H, Li D (2001) A numerical simulation of the filling stage in injection molding based on a surface model. Adv Polym Technol 20(2):125–131.
8. Himasekhar K, Lottey J, Wang KK (1992) CAE of mold cooling in injection molding using a three-dimensional numerical simulation. J EngInd Trans ASME 114(2):213–221.
9. Tang LQ, Pochiraju K, Chassapis C, Manoochehri S (1998) Computeraided optimization approach for the design of injection mold cooling systems. J Mech Des, Trans ASME 120(2):165–174.
10. Rizzo FJ, Shippy DJ (1977) An advanced boundary integral equation method for three-dimensional thermoelasticity. Int J Numer Methods Eng 11:1753–1768.
11. Hartmann F (1980) Computing the C-matrix in non-smooth boundary points. In: New developments in boundary element methods, CML Publications, Southampton, pp 367–379.
12. Chen X, Lama YC, Li DQ (2000) Analysis of thermal residual stress in plastic injection molding. J Mater Process Technol 101(1):275–280.
13. Lee EH, Rogers TG (1960) Solution of viscoelastic stress analysis problems using measured

creep or relaxation function. J Appl Mech 30(1):127–134.
14. Li Y (1997) Studies in direct tooling using stereolithography. Dissertation, University of Delaware, Newark, DE.